IEEE Access
Multidisciplinary | Rapid Review | Open Access Journal

Received December 6, 2021, accepted December 19, 2021, date of publication December 27, 2021,
date of current version January 13, 2022.

Digital Object Identifier 10.1109/ACCESS.2021.3138739

Small-Signal Stability Modeling for MMC-Based DC Grids With Voltage Slope Control and Influence Analysis of Parameters

HUI LI, XINQIAO FAN, AND SIJIA LIU
School of Automation, Beijing Information Science & Technology University, Beijing 100192, China
Corresponding author: Hui Li (lhbxy@bistu.edu.cn)

This work was supported by the Beijing Natural Science Foundation under Grant 3172015.

ABSTRACT In the flexible DC grids, selections of slope coefficients in system level controls and designs of smoothing reactors have a crucial influence on the system stability. In order to obtain their optimal values, a comprehensive small-signal stability model with the DC voltage slope control and smoothing reactors is proposed in this paper. Firstly, the linear state-space model of the entire system based on the small-signal method is deduced according to the coupling equations between the inputs, the outputs, and state variables related to converter stations and the AC sides, controllers, and the DC grid with smoothing reactors. Meanwhile, the influences of the MMC bridge arm circulating current and the capacitor voltage fluctuation of the sub-module are considered in this model. Secondly, the impacts of control parameters, smoothing reactor parameters, and bridge arm inductances are analyzed on the system stability through the Lyapunov stability theory. Finally, the simulation of Zhangbei four-terminal DC grid project in China is established to testify the correctness of the presented small-signal model and the conclusions about the impact of parameters on the system stability. The proposed method will provide some theoretical guidance for the system design and the parameter selection in DC grid applications.

INDEX TERMS DC grids, modular multilevel converter, small-signal method, slope control, smoothing reactor.

I. INTRODUCTION

With the characteristics of flexibility, economy, and reliability, the flexible DC transmission technology has become an effective means to solve the interconnection of multiple AC asynchronous power grids and large-scale renewable energy integration [1]. At present, modular multilevel converter (MMC) has become the mainstream topology of multi-terminal voltage source converter based high voltage DC transmission (VSC-MTDC) [2]–[4], due to its advantages of low switching frequency, low switching loss, low harmonic characteristics, and easy expansion of modular structures, et al [5], [6]. There have already been several MMC-MTDC projects in the world, e.g., Zhangbei four-terminal MMC-MTDC project in China [7], Zhoushan five-terminal MMC-MTDC project in China [8], TransBay Cable project [9], and so on.

The associate editor coordinating the review of this manuscript and approving it for publication was Ton Duc Do.

However, MMC is easy to cause problems such as bridge arm circulating current fluctuation and sub-module (SM) capacitor voltage unbalancing, which brings challenges to the system stability. Many scholars mainly focus on the modeling, voltage balancing and stability analysis, and so forth. In [10], the average model of MMC was deduced for analyzing terminal behaviors. Its derivation directly ignored the coupling of multiple harmonics within arms and the dynamic behavior of the SM capacitor, so it cannot accurately reflect the actual characteristic of the MMC. In [11], the sequence impedance model of MMC based on the harmonic linearization was established. In this model, the coupling among multiple harmonics within MMC and the dynamic behavior of SM capacitors were considered, but the outer-loop controller of the MMC station was not taken into account. In [12], a 10^{th}-order small-signal model of a single-terminal MMC in the d-q rotating frame was put forward, by considering the dynamic behavior of the circulating current suppressor. Other studies established a high-order small-signal model of a single-terminal MMC in [13], [14], which provided

an interface with an external controller, AC system, and DC system. In [15], the internal dynamic characteristics of MMC and DC voltage control were deduced, and a 16^{th}-order small-signal model of a single-terminal MMC was proposed. In [16], a small-signal impedance model of MMC including internal harmonic dynamics was presented for analyzing the resonance and stability of MMC-based systems. The research discussed above all focused on the stability of the single-terminal MMC system. A reduced-order model was proposed in [17] to solve the problem of high order in the MMC small-signal model, but it was only suitable for two terminal MMC-based HVDC system.

The MMC-MTDC systems have the characteristics of diverse converter types, changeable operation modes and complex control links, which makes the interaction law more complex between AC and DC system, among different control links, between DC grid and control systems. When the system fluctuates, the instability may occur. Therefore, it is necessary to study the interaction mechanism on stability analysis between AC and DC hybrid systems, so as to provide some theoretical guidance for the design and parameter selection of MMC-MTDC systems. In [18], a generic small-signal model of MMC based DC grid was established and a DC virtual impedance damping control was proposed to suppress the resonance and instability, which employed the averaged-value model of MMC. An accurate DC-side impedance modeling of MMC and a control strategy for improving the stability in MMC-based DC grid were presented in [19], which considered the coupling of internal multiple harmonics and the complete control system. These literatures all adopt the master-slave control strategy as system level controls in the stability modeling. As we know, the disadvantage of the master-slave control is that when the main converter station fails, the slave converter station can't participate the controls of the DC voltage and power flow distribution, which leads to the instability of the whole system [20].

In addition, recent researches scarcely focus on the stability of DC grids with DC equipment, such as the current-limiting reactor, smoothing reactor. It is well known that the current-limiting reactor can assist the DC circuit breaker in removing DC faults [21]–[23], and the smoothing reactor can effectively suppress the harmonics of DC current, maintain the stability of DC side voltage, and reduce the impact of DC side voltage on the converter station [24], [25]. However, such large-capacity reactors increase the electrical distance between converter stations, which adversely affect the stability of the DC grid and the control of DC voltage.

Therefore, the main contributions of this article are as follows:

1) The interaction mechanism between converter stations using the DC voltage slope control strategy and DC gird with smoothing reactors is studied in this paper.

2) A comprehensive small-signal model of the MMC-based DC grid is proposed, which includes the internal dynamic behaviors of MMCs, converter stations, diverse controllers, and the DC grid with smoothing reactors.

3) On the base of the small-signal model, the influences of slope coefficient, PI parameter, smoothing reactor parameter and bridge arm inductance on the system stability are analyzed through Lyapunov stability theory and the root locus method. Thus, a theoretical basis of the system design and the parameter selection in DC grid applications is provided.

The rest of this article is organized as follows. A comprehensive small-signal stability model for MMC-based DC grids is proposed in Section II. The influences of control parameters, smoothing reactor parameters, and bridge arm inductances are analyzed on the system stability in Section III, obtaining their reasonable value ranges that would maintain the system stability. The correctness of the presented small-signal stability model is validated by a simulated four-terminal DC grid in Section IV. Conclusions are summarized in Section V.

II. SMALL-SIGNAL STABILITY MODELING FOR MMC-BASED DC GRIDS

A. SMALL-SIGNAL MODELING OF CONVERTER STATIONS AND AC SIDES

In this paper, the mathematical model of the converter station is obtained by considering the influence of the circulating current and the SM capacitor voltage fluctuation. Fig.1 shows the basic structure of the MMC station.

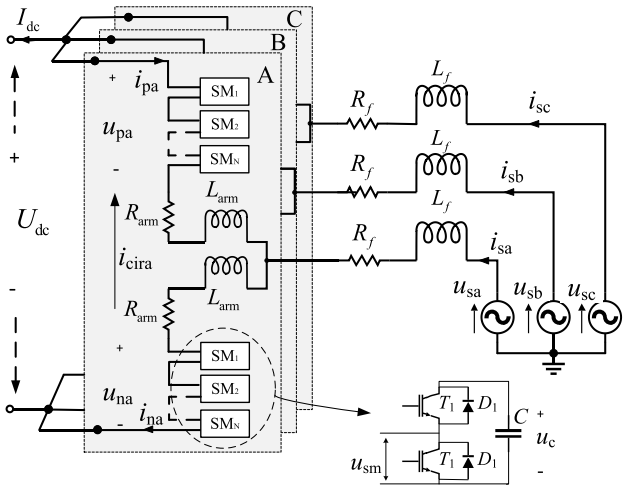

FIGURE 1. The basic structure of the MMC station.

In Fig.1, the SM adopts a semi-half-bridge structure. u_{pa} and u_{na} are the voltages of the upper and lower bridge arms, respectively. i_{pa} and i_{na} are the currents of the upper and lower bridge arm, respectively. R_{arm} and L_{arm} are the resistance and inductance of the bridge arm, respectively. R_f and L_f are the equivalent resistance and inductance for the AC side, respectively. i_{cira} is the circulating current of phase A bridge arm. U_{dc} and I_{dc} are the voltage and current of the DC side, respectively. u_s and i_s are the voltage and the current of the AC side, respectively. The subscript N is the number of SM in each bridge arm.

Take phase A as an example to establish the small-signal model between the converter station and the AC side. As considering the influences of the bridge arm circulating currents, the current i_{pa} and i_{na} are composed of the DC component, the fundamental frequency component and the double frequency circulating current component, ignoring the high-order circulating current components. The instantaneous value of the bridge arm current can be expressed as follows.

$$\begin{cases} i_{pa} = \frac{1}{3}I_{dc} - \frac{1}{2}I_{sa}\sin(\omega t + \beta_1) + I_{cira}\sin(2\omega t + \beta_2) \\ i_{na} = \frac{1}{3}I_{dc} + \frac{1}{2}I_{sa}\sin(\omega t + \beta_1) + I_{cira}\sin(2\omega t + \beta_2) \end{cases} \tag{1}$$

where I_{sa} and β_1 are the amplitude and the phase angle of the fundamental frequency component, respectively. I_{cira} and β_2 are the amplitude and the phase angle of the double frequency circulating current component, respectively.

Meanwhile, the SM capacitor voltage fluctuations are considered. The SM capacitor voltage u_{ca} of the upper bridge arm at phase A is composed of the DC component U_{c_dc}, the fundamental frequency component u_{ca_ac1} and the double frequency component u_{ca_ac2}, ignoring the components above triple frequency. The instantaneous value of the SM capacitor voltage can be expressed as follows.

$$u_{ca} = U_{c\_dc} + U_{ca\_ac1}\sin(\omega t + \theta_1) + U_{ca\_ac2}\sin(2\omega t + \theta_2) \tag{2}$$

where U_{ca_ac1} and θ_1 are the amplitude and the phase angle of the fundamental frequency component, respectively. U_{ca_ac2} and θ_2 are the amplitude and the phase angle of the double frequency component, respectively.

If there are enough SMs of each bridge arm, the output voltage of the bridge arm can be considered continuous. Taking the upper bridge arm at phase A as an example, its average switching function model can be expressed as

$$\begin{cases} S_p \cdot i_{pa} = C\frac{du_{ca}}{dt} \\ u_{pa} = N \cdot S_p \cdot u_{ca} \end{cases} \tag{3}$$

where C is the capacitance of the SM. S_p is the average switching function of the upper bridge arm, namely

$$S_p = \frac{1}{2} - \frac{1}{2}M\sin(\omega t + \alpha) + \frac{U_{cira}}{U_{dc}}\sin(2\omega t + \varphi) \tag{4}$$

where M and α are the modulation ratio and the phase angle of the fundamental frequency reference voltage, respectively. U_{cira} and φ are the amplitude and the phase angle of the voltage correction component in the circulating current suppressor, respectively.

Substituting Eq. (1) and Eq. (4) into Eq. (3), the dynamic equations of DC component, fundamental frequency component and double frequency component of the SM capacitor voltage are obtained in Eq. (5).

$$\begin{cases} \frac{dU_{c\_dc}}{dt} = \frac{1}{6C}I_{dc} + \frac{U_{cira}I_{cira}}{2CU_{dc}}\cos(\varphi - \beta_2) \\ \quad + \frac{1}{8C}MI_{sa}\cos(\alpha - \beta_1) \\ \frac{dU_{ca\_ac1}}{dt} = -\frac{1}{4C}I_{sa}\sin(\omega t + \beta_1) \\ \quad - \frac{1}{4C}MI_{cira}\cos(\omega t + \beta_2 - \alpha) \\ -\frac{1}{6C}MI_{dc}\sin(\omega t + \alpha) - \frac{1}{4C}\frac{U_{cira}I_{sa}}{U_{dc}}\cos(\omega t + \varphi - \beta_1) \\ \frac{dU_{ca\_ac2}}{dt} = -\frac{1}{8C}MI_{sa}\cos(2\omega t + \alpha + \beta_1) \\ \quad + \frac{1}{2C}I_{cira}\sin(2\omega t + \beta_2) + \frac{U_{cira}I_{dc}}{3CU_{dc}}\sin(2\omega t + \varphi) \end{cases} \tag{5}$$

Combined with the three-phase expressions of Eq. (5), the state equations of the SM capacitor voltage represented by d-q component are obtained in Eq. (6) after d-q transforms of positive-sequence fundamental frequency and negative-sequence double frequency, respectively.

$$\begin{cases} \frac{dU_{c\_dc}}{dt} = \frac{I_{dc}}{6C} + \frac{U_{c1d}I_{sd}}{4CU_{dc}} + \frac{U_{c1q}I_{sq}}{4CU_{dc}} + \frac{U_{cird}I_{cird}}{2CU_{dc}} \\ \quad + \frac{U_{cirq}I_{cirq}}{2CU_{dc}} \\ \frac{dU_{c\_d1}}{dt} = -\omega U_{c\_q1} - \frac{U_{c1d}I_{dc}}{3CU_{dc}} - \frac{I_{sd}}{4C} - \frac{U_{cird}I_{sd}}{4CU_{dc}} \\ \quad - \frac{U_{cirq}I_{sq}}{4CU_{dc}} - \frac{U_{c1d}I_{cird}}{2CU_{dc}} - \frac{U_{c1q}I_{cirq}}{2CU_{dc}} \\ \frac{dU_{c\_q1}}{dt} = \omega U_{c\_d1} - \frac{U_{c1q}I_{dc}}{3CU_{dc}} - \frac{U_{cirq}I_{sd}}{4CU_{dc}} + \frac{U_{cird}I_{sq}}{4CU_{dc}} - \frac{I_{sq}}{4C} \\ \quad + \frac{U_{c1q}I_{cird}}{2CU_{dc}} - \frac{U_{c1d}I_{cirq}}{2CU_{dc}} \\ \frac{dU_{c\_d2}}{dt} = -2\omega U_{c\_q2} + \frac{U_{cird}I_{dc}}{3CU_{dc}} + \frac{U_{c1d}I_{sd}}{4CU_{dc}} - \frac{U_{c1q}I_{sq}}{4CU_{dc}} \\ \quad + \frac{I_{cird}}{2C} \\ \frac{dU_{c\_q2}}{dt} = 2\omega U_{c\_d2} + \frac{U_{cirq}I_{dc}}{3CU_{dc}} - \frac{U_{c1q}I_{sd}}{4CU_{dc}} + \frac{U_{c1d}I_{sq}}{4CU_{dc}} \\ \quad + \frac{I_{cirq}}{2C} \end{cases} \tag{6}$$

where U_{c_1d} and U_{c_1q} represent the d-q components of the fundamental frequency component U_{ca_ac1}, respectively. U_{c_2d} and U_{c_2q} represent the d-q components of the double frequency component U_{ca_ac2}, respectively. U_{sd}, U_{sq}, I_{sd}, I_{sq} represent the d-q components of the voltage and the current at the AC side, respectively. I_{cird} and I_{cirq} represent the d-q components of the double-frequency circulating current. U_{cird} and U_{cirq} represent the d-q components of the double-frequency modulation voltage output by the circulating current suppressor. U_{c1d} and U_{c1q} are the d-q components of the three-phase fundamental frequency reference voltages, namely

$$\begin{cases} U_{c1d} = MU_{dc}\sin\alpha/2 \\ U_{c1q} = MU_{dc}\cos\alpha/2 \end{cases}$$

Substituting Eq. (2) and Eq. (4) into Eq. (3), the DC component $U_{\mathrm{pa\_dc}}$, the fundamental frequency component$u_{\mathrm{pa_ac1}}$ and the double frequency component $u_{\mathrm{pa\_ac2}}$ of the upper bridge arm voltage are obtained in Eq. (7), ignoring the components above triple frequency.

$$\begin{cases} U_{\mathrm{pa\_dc}} = \dfrac{1}{2}NU_{\mathrm{c\_dc}} - \dfrac{1}{4}NMU_{\mathrm{ca\_ac1}}\cos(\alpha-\theta_1) \\ -\dfrac{U_{\mathrm{cira}}}{2U_{\mathrm{dc}}}NU_{\mathrm{ca\_ac2}}\cos(\varphi-\theta_2) \\ u_{\mathrm{pa\_ac1}} = -\dfrac{1}{2}NMU_{\mathrm{c\_dc}}\sin(\omega t+\alpha)+\dfrac{1}{2}NU_{\mathrm{ca\_ac1}}\sin(\omega t+\theta_1) \\ +\dfrac{U_{\mathrm{cira}}}{2U_{\mathrm{dc}}}NU_{\mathrm{ca\_ac1}}\cos(\omega t+\varphi-\theta_1) \\ -\dfrac{1}{4}NMU_{\mathrm{ca\_ac2}}\cos(\omega t+\theta_2-\alpha) \\ u_{\mathrm{pa\_ac2}} = \dfrac{U_{\mathrm{cira}}}{U_{\mathrm{dc}}}NU_{\mathrm{c\_dc}}\sin(2\omega t+\varphi)+\dfrac{1}{2}NU_{\mathrm{ca\_ac2}}\sin(2\omega t+\theta_2) \\ +\dfrac{1}{4}NMU_{\mathrm{ca\_ac1}}\cos(2\omega t+\theta_1+\alpha) \end{cases} \tag{7}$$

According to the KVL, the voltage equations related to the DC side and the AC side of the converter in Fig. 1 can be expressed as follows.

$$\begin{cases} U_{\mathrm{dc}} = 2U_{\mathrm{pa\_dc}} + \dfrac{2}{3}R_{\mathrm{arm}}I_{\mathrm{dc}} + \dfrac{2}{3}L_{\mathrm{arm}}\dfrac{\mathrm{d}I_{\mathrm{dc}}}{\mathrm{d}t} \\ u_{\mathrm{sa}} = -u_{\mathrm{pa\_c1}} + L_{\mathrm{eq}}\dfrac{\mathrm{d}i_{\mathrm{sa}}}{\mathrm{d}t} + R_{\mathrm{eq}}i_{\mathrm{sa}} \\ 2u_{\mathrm{pa\_c2}} + 2L_{\mathrm{arm}}\dfrac{\mathrm{d}i_{\mathrm{cira}}}{\mathrm{d}t} + 2R_{\mathrm{arm}}i_{\mathrm{cira}} = 0 \end{cases} \tag{8}$$

where $L_{\mathrm{eq}} = L_{\mathrm{f}} + L_{\mathrm{arm}}/2$, $R_{\mathrm{eq}} = R_{\mathrm{f}} + R_{\mathrm{arm}}/2$.

Substituting Eq. (7) into Eq. (8), the state equations of the DC side current, the AC side current and the circulating current related to phase A can be expressed in Eq. (9).

$$\begin{cases} \dfrac{\mathrm{d}I_{\mathrm{dc}}}{\mathrm{d}t} = \dfrac{3U_{\mathrm{dc}}}{2L_{\mathrm{arm}}} - \dfrac{R_{\mathrm{arm}}I_{\mathrm{dc}}}{L_{\mathrm{arm}}} - \dfrac{3NU_{\mathrm{c\_dc}}}{2L_{\mathrm{arm}}} \\ \quad -\dfrac{3NMU_{\mathrm{ca\_ac1}}\cos(\alpha-\theta_1)}{4L_{\mathrm{arm}}} \\ +\dfrac{3NU_{\mathrm{cira}}U_{\mathrm{ca\_ac2}}\cos(\varphi-\theta_2)}{2L_{\mathrm{arm}}U_{\mathrm{dc}}} \\ \dfrac{\mathrm{d}i_{\mathrm{sa}}}{\mathrm{d}t} = \dfrac{1}{L_{\mathrm{eq}}}u_{\mathrm{sa}} - \dfrac{R_{\mathrm{eq}}}{L_{\mathrm{eq}}}i_{\mathrm{sa}} - \dfrac{NMU_{\mathrm{c\_dc}}\sin(\omega t+\alpha)}{2L_{\mathrm{eq}}} \\ +\dfrac{NU_{\mathrm{ca\_ac1}}\sin(\omega t+\theta_1)}{2L_{\mathrm{eq}}} \\ +\dfrac{NU_{\mathrm{cira}}U_{\mathrm{ca\_ac1}}\cos(\omega t+\varphi-\theta_1)}{2L_{\mathrm{eq}}U_{\mathrm{dc}}} \\ -\dfrac{NMU_{\mathrm{ca\_ac2}}\cos(\omega t+\theta_2-\alpha)}{4L_{\mathrm{eq}}} \\ \dfrac{\mathrm{d}i_{\mathrm{cira}}}{\mathrm{d}t} = -\dfrac{R_{\mathrm{arm}}}{L_{\mathrm{arm}}}i_{\mathrm{cira}} - \dfrac{NU_{\mathrm{cira}}U_{\mathrm{c\_dc}}\sin(2\omega t+\varphi)}{L_{\mathrm{arm}}U_{\mathrm{dc}}} \\ -\dfrac{NMU_{\mathrm{ca\_ac1}}\cos(2\omega t+\theta_1+\alpha)}{4L_{\mathrm{arm}}} \\ -\dfrac{NU_{\mathrm{ca\_ac2}}\sin(2\omega t+\theta_2)}{2L_{\mathrm{arm}}} \end{cases} \tag{9}$$

Combined with the three-phase expressions of Eq. (9), the station equations of the DC side current, the AC side current and the circulating current represented by d-q component are obtained after d-q transforms of positive-sequence fundamental frequency and negative-sequence double frequency, respectively.

$$\begin{cases} \dfrac{\mathrm{d}I_{\mathrm{dc}}}{\mathrm{d}t} = -\dfrac{3NU_{\mathrm{c\_dc}}}{2L_{\mathrm{arm}}} + \dfrac{3NU_{\mathrm{c1}d}U_{\mathrm{c\_1}d}}{2L_{\mathrm{arm}}U_{\mathrm{dc}}} + \dfrac{3NU_{\mathrm{c1}q}U_{\mathrm{c\_1}q}}{2L_{\mathrm{arm}}U_{\mathrm{dc}}} \\ \quad -\dfrac{3NU_{\mathrm{cird}}U_{\mathrm{c\_2}d}}{2L_{\mathrm{arm}}U_{\mathrm{dc}}} \\ \quad -\dfrac{3NU_{\mathrm{cirq}}U_{\mathrm{c\_2}q}}{2L_{\mathrm{arm}}U_{\mathrm{dc}}} - \dfrac{R_{\mathrm{arm}}I_{\mathrm{dc}}}{L_{\mathrm{arm}}} + \dfrac{3U_{\mathrm{dc}}}{2L_{\mathrm{arm}}} \\ \dfrac{\mathrm{d}I_{\mathrm{sd}}}{\mathrm{d}t} = -N\dfrac{2U_{\mathrm{c\_dc}}U_{\mathrm{c1}d}}{2L_{\mathrm{eq}}} + \dfrac{NU_{\mathrm{c\_1}d}}{2L_{\mathrm{eq}}} \\ \quad +N\dfrac{U_{\mathrm{cirq}}U_{\mathrm{c1q}} + U_{\mathrm{cird}}U_{\mathrm{c\_1}d}}{2L_{\mathrm{eq}}U_{\mathrm{dc}}} \\ \quad -N\dfrac{U_{\mathrm{c1}d}U_{\mathrm{c\_2}d} + U_{\mathrm{c1q}}U_{\mathrm{c\_2}q}}{2L_{\mathrm{eq}}} - \omega I_{\mathrm{sq}} - \dfrac{R_{\mathrm{eq}}}{L_{\mathrm{eq}}}I_{\mathrm{sd}} + \dfrac{U_{\mathrm{sd}}}{L_{\mathrm{eq}}} \\ \dfrac{\mathrm{d}I_{\mathrm{sq}}}{\mathrm{d}t} = -N\dfrac{2U_{\mathrm{c\_dc}}U_{\mathrm{c1}q}}{2L_{\mathrm{eq}}} + \dfrac{NU_{\mathrm{c\_1q}}}{2L_{\mathrm{eq}}} \\ \quad +N\dfrac{U_{\mathrm{cirq}}U_{\mathrm{c1d}} - U_{\mathrm{cird}}U_{\mathrm{c\_1q}}}{2L_{\mathrm{eq}}U_{\mathrm{dc}}} \\ \quad -N\dfrac{U_{\mathrm{c1d}}U_{\mathrm{c\_2q}} - U_{\mathrm{c1q}}U_{\mathrm{c\_2d}}}{2L_{\mathrm{eq}}} + \omega I_{\mathrm{sq}} - \dfrac{R_{\mathrm{eq}}}{L_{\mathrm{eq}}}I_{\mathrm{sq}} + \dfrac{U_{\mathrm{sq}}}{L_{\mathrm{eq}}} \\ \dfrac{\mathrm{d}I_{\mathrm{cird}}}{\mathrm{d}t} = -\dfrac{NU_{\mathrm{c\_dc}}U_{\mathrm{cird}}}{L_{\mathrm{arm}}U_{\mathrm{dc}}} + N\dfrac{U_{\mathrm{c1d}}U_{\mathrm{c\_1d}} - U_{\mathrm{c1q}}U_{\mathrm{c\_1q}}}{2L_{\mathrm{arm}}U_{\mathrm{dc}}} \\ -\dfrac{NU_{\mathrm{c\_2d}}}{2L_{\mathrm{arm}}} - 2\omega I_{\mathrm{cirq}} - \dfrac{R_{\mathrm{arm}}}{L_{\mathrm{arm}}}I_{\mathrm{cird}} \\ \dfrac{\mathrm{d}I_{\mathrm{cirq}}}{\mathrm{d}t} = -\dfrac{NU_{\mathrm{c\_dc}}U_{\mathrm{cirq}}}{L_{\mathrm{arm}}U_{\mathrm{dc}}} + N\dfrac{U_{\mathrm{c1d}}U_{\mathrm{c\_1q}} + U_{\mathrm{c1q}}U_{\mathrm{c\_1d}}}{2L_{\mathrm{arm}}U_{\mathrm{dc}}} \\ -\dfrac{NU_{\mathrm{c\_2q}}}{2L_{\mathrm{arm}}} + 2\omega I_{\mathrm{cird}} - \dfrac{R_{\mathrm{arm}}}{L_{\mathrm{arm}}}I_{\mathrm{cirq}} \end{cases} \tag{10}$$

Combined with Eq. (6) and Eq. (10), the 10^{th}-order small-signal model of the single-ended MMC station after linearization at a certain steady-state operation point is obtained in Eq. (11).

$$\begin{cases} \Delta\dot{\boldsymbol{x}}_{\mathrm{s}} = \boldsymbol{A}_{\mathrm{s}}\Delta\boldsymbol{x}_{\mathrm{s}} + \boldsymbol{B}_{\mathrm{s}}\Delta\boldsymbol{u}_{\mathrm{s}} \\ \Delta\boldsymbol{y}_{\mathrm{s}} = \boldsymbol{C}_{\mathrm{s}}\Delta\boldsymbol{x}_{\mathrm{s}} + \boldsymbol{D}_{\mathrm{s}}\Delta\boldsymbol{u}_{\mathrm{s}} \end{cases} \tag{11}$$

where the state variable matrix and the input variable matrix are shown, namely

$$\Delta\boldsymbol{x}_{\mathrm{s}} = \left[\Delta U_{\mathrm{c\_dc}}\ \Delta U_{\mathrm{c\_1d}}\ \Delta U_{\mathrm{c\_1q}}\ \Delta U_{\mathrm{c\_2d}}\ \Delta U_{\mathrm{c\_2q}}\ \Delta I_{\mathrm{dc}}\ \Delta I_{\mathrm{sd}}\ \Delta I_{\mathrm{sq}}\ \Delta I_{\mathrm{cird}}\ \Delta I_{\mathrm{cirq}}\right]^T$$

$$\Delta\boldsymbol{u}_{\mathrm{s}} = \left[\Delta U_{\mathrm{c1d}}\Delta U_{\mathrm{c1q}}\Delta U_{\mathrm{cird}}\ \Delta U_{\mathrm{cirq}}\ \Delta\omega\Delta U_{\mathrm{sd}}\ \Delta U_{\mathrm{sq}}\ \Delta U_{\mathrm{dc}}\right]^T$$

$$\Delta\boldsymbol{y}_{\mathrm{s}} = \left[\Delta I_{\mathrm{sd}}\ \Delta I_{\mathrm{sq}}\ \Delta I_{\mathrm{cird}}\ \Delta I_{\mathrm{ctrq}}\ \Delta U_{\mathrm{sd}}\ \Delta U_{\mathrm{sq}}\ \ \Delta U_{\mathrm{dc}}\ \Delta I_{\mathrm{dc}}\right]^T.$$

where the input variables ΔU_{sd} and ΔU_{sq} provide an interface to the AC system. The input variable ΔU_{dc} provides an interface to the DC side. The input variable $\Delta\omega$ provide an interface to the PLL controller. The input variables $\Delta U_{\mathrm{c1}d}$ and ΔU_{c1q} provide an interface to the main controller. The input variables ΔU_{cird} and ΔU_{cirq} provide an interface to the circulating current suppressor.

B. SMALL-SIGNAL MODELING OF CONTROL SYSTEMS

1) MODELING OF THE DC VOLTALGE SLOPE CONTROLLER

In the MMC-MTDC transmission system, the DC voltage slope control is increasingly being used to realize DC voltage coordinated control among multiple converter stations. It is superior to the master-slave control, because there is no need to switch the working modes of MMC, and no communication between stations either [26]. However, inappropriate slope coefficients will have a certain influence on the system stability. In this paper, a small-signal model based on the DC voltage slope control strategy is proposed for the slope coefficient setting. Fig. 2 shows the structure of the main controller based on DC voltage slope control.

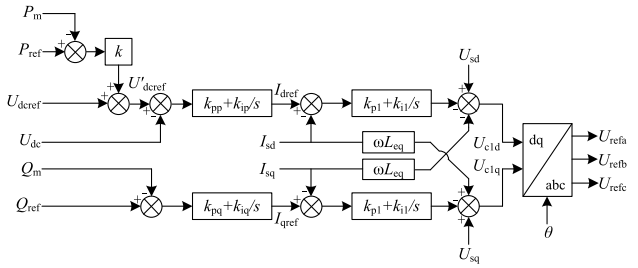

FIGURE 2. Structure of the main controller based on DC voltage slope control.

where P_{ref} and P_m are the reference and the measured values of active power, respectively. Q_{ref} and Q_m are the reference and the measured values of reactive power, respectively. U_{dcref} is the reference value of DC voltage. I_{dref} and I_{qref} are the reference values of d-q current component entering the inner loop controller, respectively. U_{refa}, U_{refb} and U_{refc} are the three-phase modulation voltages after the Park inverse transform. k is the coefficient of DC voltage slope control.

At this time, the influences of coefficient k and the active power deviation are considered to the outer loop controller. For the two integral elements of the outer loop in Fig.2, two state variables are introduced, respectively.

$$\begin{cases} x_1 = \int \left(U'_{dcref} - U_{dc}\right) dt \Rightarrow \dfrac{dx_1}{dt} = U'_{dcref} - U_{dc} \\ x_2 = \int \left(Q_{ref} - Q_m\right) dt \Rightarrow \dfrac{dx_2}{dt} = Q_{ref} - Q_m \end{cases} \tag{12}$$

where U'_{dcref} is the revised value of U_{dcref} after the slope control, namely

$$U'_{dcref} = U_{dcref} + k(P_{ref} - P_m)$$

The active power P_m and the reactive power Q_m can be expressed as follows.

$$\begin{cases} P_m = \dfrac{3}{2}\left(U_{sd}I_{sd} + U_{sq}I_{sq}\right) \\ Q_m = \dfrac{3}{2}\left(U_{sd}I_{sq} - U_{sq}I_{sd}\right) \end{cases} \tag{13}$$

The reference values of the inner loop currents are the outputs of the outer loop controller, and their expressions are as follows.

$$\begin{cases} I_{dref} = k_{pp}[U'_{dcref} - U_{dc}] + k_{ip}x_1 \\ I_{qref} = k_{pq}(Q_{ref} - Q_m) + k_{iq}x_2 \end{cases} \tag{14}$$

where k_{pp} and k_{pq} are the proportional gains of the outer loop controller. k_{ip} and k_{iq} are the integral gains of the outer loop controller.

For the two integral elements of the inner loop in Fig.2, two state variables are introduced, respectively.

$$\begin{cases} \dfrac{dx_3}{dt} = I_{dref} - I_{sd} \\ \dfrac{dx_4}{dt} = I_{qref} - I_{sq} \end{cases} \tag{15}$$

The outputs of the main controller (namely the inputs of the MMC model) in Fig. 2 can be expressed as

$$\begin{cases} U_{c1d} = U_{sd} - \omega L_{eq}I_{sq} - [k_{p1}(I_{dref} - I_{sd}) + k_{i1}x_3] \\ U_{c1q} = U_{sq} + \omega L_{eq}I_{sd} - [k_{p1}(I_{qref} - I_{sq}) + k_{i1}x_4] \end{cases} \tag{16}$$

where k_{p1} and k_{i1} are the proportional and the integral gain of the inner loop controller, respectively.

2) MODELING OF THE CIRCULATING CURRENT SUPPRESSOR

As the special structure and the modulation mode of MMC lead to the inconsistency between the voltages of the upper and lower bridge arms, and form the internal circulations which cause the distortion of the bridge arm currents. The circulating current suppressor is introduced to weaken the double frequency negative-sequence circulating current and reduce the loss of the converter. The structure of the circulating current suppressor is shown in Fig.3.

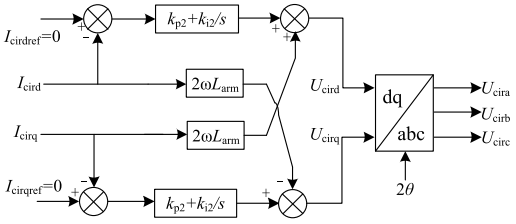

FIGURE 3. Structure of the circulating current suppressor.

where $I_{cirdref}$ and $I_{cirqref}$ are the d-q reference values of the double frequency circulating current, respectively. U_{cira}, U_{cirb} and U_{circ} are the three-phase modulation voltages after the Park inverse transform, respectively. The modulation voltage U_{cira}, U_{cirb} and U_{circ} of the circulating current suppressor and the modulation voltage U_{refa}, U_{refb}, U_{refc} of the main controller are added to generate the trigger signal of six bridge arms for controlling switch on and off in the SM by using the nearest level approximation strategy.

For the two integral elements of PI controls in Fig.3, two state variables are introduced, respectively.

$$\begin{cases} \dfrac{\mathrm{d}f_1}{\mathrm{d}t} = I_{\mathrm{cirdref}} - I_{\mathrm{cird}} \\ \dfrac{\mathrm{d}f_2}{\mathrm{d}t} = I_{\mathrm{cirqref}} - I_{\mathrm{cirq}} \end{cases} \tag{17}$$

The outputs of the circulating current suppressor (namely the inputs of the MMC model) can be expressed as follows.

$$\begin{cases} U_{\mathrm{cird}} = 2\omega L_{\mathrm{arm}} I_{\mathrm{cirq}} + k_{\mathrm{p2}}(I_{\mathrm{cirdref}} - I_{\mathrm{cird}}) + k_{\mathrm{i2}} f_1 \\ U_{\mathrm{cirq}} = -2\omega L_{\mathrm{arm}} I_{\mathrm{cird}} + k_{\mathrm{p2}}(I_{\mathrm{cirqref}} - I_{\mathrm{cirq}}) + k_{\mathrm{i2}} f_2 \end{cases} \tag{18}$$

where k_{p2} and k_{i2} are the proportional and integral gain of the circulating current suppressor, respectively.

The state space model of the converter station control system is obtained according to Eq. (12) $\sim$ Eq. (18), and its small-signal model after linearization is shown as follows.

$$\begin{cases} \Delta\dot{\boldsymbol{x}}_{\mathrm{c}} = \boldsymbol{A}_{\mathrm{c}}\Delta\boldsymbol{x}_{\mathrm{k}} + \boldsymbol{B}_{\mathrm{c}}\Delta\boldsymbol{u}_{\mathrm{c}} \\ \Delta\boldsymbol{y}_{\mathrm{c}} = \boldsymbol{C}_{\mathrm{c}}\Delta\boldsymbol{x}_{\mathrm{c}} + \boldsymbol{D}_{\mathrm{c}}\Delta\boldsymbol{u}_{\mathrm{c}} \end{cases} \tag{19}$$

where;

$$\begin{aligned} \Delta\boldsymbol{x}_{\mathrm{c}} &= [\Delta f_1, \Delta f_2, \Delta x_1, \Delta x_2, \Delta x_3, \Delta x_4]^T; \\ \Delta\boldsymbol{u}_{\mathrm{c}} &= \big[\Delta I_{\mathrm{sd}}\ \Delta I_{\mathrm{sq}}\ \Delta I_{\mathrm{cird}}\ \Delta I_{\mathrm{ctrq}}\ \Delta U_{\mathrm{sd}}\ \Delta U_{\mathrm{sq}} \\ &\quad \Delta U_{\mathrm{dc}}\ \Delta P_{\mathrm{ref}}\ \Delta Q_{\mathrm{ref}}\ \ \Delta U_{\mathrm{dcref}}\big]^T; \\ \Delta\boldsymbol{y}_{\mathrm{c}} &= \big[\Delta U_{\mathrm{c1d}}, \Delta U_{\mathrm{c1q}}, \Delta U_{\mathrm{cird}}, \Delta U_{\mathrm{cirq}}\big]^T. \end{aligned}$$

Thus, the small-signal model of the single-ended MMC station is obtained by combining Eq. (11) and Eq. (19) as follows.

$$\Delta\dot{\boldsymbol{x}}_{\mathrm{m}} = \boldsymbol{A}_{\mathrm{m}}\Delta\boldsymbol{x}_{\mathrm{m}} + \boldsymbol{B}_{\mathrm{m}}\Delta\boldsymbol{u}_{\mathrm{m}} \tag{20}$$

where

$$\Delta\boldsymbol{x}_{\mathrm{m}} = [\Delta\boldsymbol{x}_{\mathrm{s}}, \Delta\boldsymbol{x}_{\mathrm{c}}]^T,\ \Delta\boldsymbol{u}_{\mathrm{m}} = [\Delta\boldsymbol{u}_{\mathrm{s1}}, \Delta\boldsymbol{u}_{\mathrm{c2}}]^T,$$

$$\boldsymbol{A}_{\mathrm{m}} = \begin{bmatrix} \boldsymbol{A}_{\mathrm{s}} + \boldsymbol{B}_{\mathrm{s2}}\boldsymbol{D}_{\mathrm{c1}}\boldsymbol{E} & \boldsymbol{B}_{\mathrm{s2}}\boldsymbol{C}_{\mathrm{c}} \\ \boldsymbol{B}_{\mathrm{c1}}\boldsymbol{E} & \boldsymbol{A}_{c} \end{bmatrix},\ \boldsymbol{B}_{\mathrm{m}} = \begin{bmatrix} \boldsymbol{B}_{\mathrm{s1}} & \boldsymbol{B}_{\mathrm{s2}}\boldsymbol{D}_{\mathrm{c2}} \\ \boldsymbol{0} & \boldsymbol{B}_{\mathrm{c2}} \end{bmatrix},$$

$$\boldsymbol{E} = \begin{bmatrix} 0&0&0&0&0&0&1&0&0&0 \\ 0&0&0&0&0&0&0&1&0&0 \\ 0&0&0&0&0&0&0&0&1&0 \\ 0&0&0&0&0&0&0&0&0&1 \end{bmatrix}.$$

$\Delta\boldsymbol{u}_{s1}$ is the first four variables of $\Delta\boldsymbol{u}_{s}$. $\Delta\boldsymbol{u}_{c2}$ is the last six variables of $\Delta\boldsymbol{u}_{c}$. $\boldsymbol{B}_{s1}$ is the first four columns of $\boldsymbol{B}_{s}$, and $\boldsymbol{B}_{s2}$ is the last four columns of $\boldsymbol{B}_{s}$. $\boldsymbol{B}_{c1}$ is the first four columns of $\boldsymbol{B}_{c}$, and $\boldsymbol{B}_{c2}$ is the last six columns of $\boldsymbol{B}_{c}$. $\boldsymbol{D}_{c1}$ is the first four columns of $\boldsymbol{D}_{c}$, and $\boldsymbol{D}_{c2}$ is the last six columns of $\boldsymbol{D}_{c}$.

C. SMALL-SIGNAL MODELING OF DC TRANSMISSION LINES WITH SMOOTHING REACTORS

Fig. 4 is the single-pole diagram of Zhangbei four-terminal flexible DC grid with smoothing reactors, in which Kangbao station and Zhangbei station are sending terminals, Fengning station is a regulating terminal and Beijing station is a receiving terminal. In order to determine the optimal value of the smoothing reactor taking into account both the harmonic current suppression and the system stability, a small-signal model of DC lines with smoothing reactors is built.

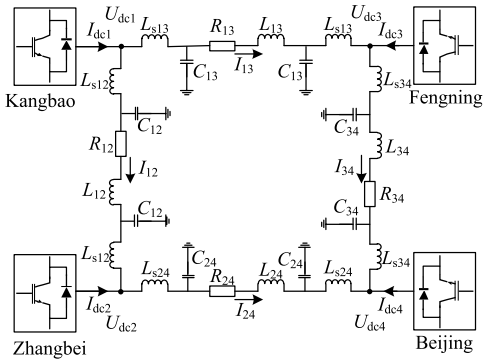

FIGURE 4. The single-pole diagram of Zhangbei four-terminal DC grid.

In Fig. 4, U_{dcj} and I_{dcj} are the voltage and the current at the DC side of the j-th MMC station, j = 1,2,3,4. L_{s12}, L_{s13}, L_{s24} and L_{s34} are the smoothing reactors on the DC lines. For simplifying analysis, the π-type model expressed by lumped parameters is used to simulate the DC lines. Considering that the smoothing reactor has no DC voltage drop in the steady state, the grounded capacitances of the two lines connecting to the same MMC station are combined to get the simplified form of state-space equations. For example, the state-space equations about the current I_{13} and the voltage U_{dc1} are expressed as follows, according to KCL and KVL.

$$\begin{cases} \dfrac{\mathrm{d}I_{13}}{\mathrm{d}t} = \dfrac{1}{2L_{s13} + L_{13}}(-I_{13}R_{13} + U_{\mathrm{dc1}} - U_{\mathrm{dc3}}) \\ \dfrac{\mathrm{d}U_{\mathrm{dc1}}}{\mathrm{d}t} = \dfrac{1}{C_{12} + C_{13}}(I_{\mathrm{dc1}} - I_{12} - I_{13}) \end{cases}$$

Then, a small-signal model of four-terminal equivalent DC power grid can be deduced in Eq. (21).

$$\begin{cases} \Delta\dot{\boldsymbol{x}}_{\mathrm{g}} = \boldsymbol{A}_{\mathrm{g}}\Delta\boldsymbol{x}_{\mathrm{g}} + \boldsymbol{B}_{\mathrm{g}}\Delta\boldsymbol{u}_{\mathrm{g}} \\ \Delta\boldsymbol{y}_{\mathrm{g}} = \boldsymbol{C}_{\mathrm{g}}\Delta\boldsymbol{x}_{\mathrm{g}} + \boldsymbol{D}_{\mathrm{g}}\Delta\boldsymbol{u}_{\mathrm{g}} \end{cases} \tag{21}$$

where $\Delta\boldsymbol{x}_{\mathrm{g}} = \big[\ \Delta\boldsymbol{I}_{\mathrm{L}}\ \Delta\boldsymbol{U}_{\mathrm{dc}}\ \big]^{\mathrm{T}}$ is the state variable $\Delta\boldsymbol{I}_{\mathrm{L}}$, $\Delta\boldsymbol{y}_{\mathrm{g}}$, $\Delta\boldsymbol{u}_{\mathrm{g}}$, $\boldsymbol{A}_{\mathrm{g}}$–$\boldsymbol{D}_{\mathrm{g}}$, and $\boldsymbol{F}_1$–$\boldsymbol{F}_4$, as shown at the bottom of the next page.

Finally, a comprehensive small-signal stability model for MMC-based DC grids is established by combining Eq. (20) and Eq. (21), considering the internal dynamic characteristics of the MMC, the DC voltage slope control, the function of the circulating current suppressor and the smoothing reactors. The block form of the model is shown in Eq. (22).

$$\begin{bmatrix} \Delta\dot{\boldsymbol{x}}_{\mathrm{m1}} \\ \Delta\dot{\boldsymbol{x}}_{\mathrm{m2}} \\ \Delta\dot{\boldsymbol{x}}_{\mathrm{m3}} \\ \Delta\dot{\boldsymbol{x}}_{\mathrm{m4}} \\ \Delta\dot{\boldsymbol{x}}_{\mathrm{g}} \end{bmatrix}$$

$$= \left[\begin{array}{cccc|c} \boldsymbol{A}_{\mathrm{m1}} & & & & \\ & \boldsymbol{A}_{\mathrm{m2}} & & & \\ & & \boldsymbol{A}_{\mathrm{m3}} & & \boldsymbol{A}_1 \\ & & & \boldsymbol{A}_{\mathrm{m4}} & \\ \hline & & \boldsymbol{A}_2 & & \boldsymbol{A}_{\mathrm{g}} \end{array}\right] \left[\begin{array}{c} \Delta\boldsymbol{x}_{\mathrm{m1}} \\ \Delta\boldsymbol{x}_{\mathrm{m2}} \\ \Delta\boldsymbol{x}_{\mathrm{m3}} \\ \Delta\boldsymbol{x}_{\mathrm{m4}} \\ \Delta\boldsymbol{x}_{\mathrm{g}} \end{array}\right] + \left[\begin{array}{cccc|c} \boldsymbol{B}_{\mathrm{m1}} & & & & \\ & \boldsymbol{B}_{\mathrm{m2}} & & & \\ & & \boldsymbol{B}_{\mathrm{m3}} & & \boldsymbol{B}_1 \\ & & & \boldsymbol{B}_{\mathrm{m4}} & \\ \hline & & \boldsymbol{B}_2 & & \boldsymbol{B}_{\mathrm{g}} \end{array}\right] \left[\begin{array}{c} \Delta\boldsymbol{u}_{\mathrm{m1}} \\ \Delta\boldsymbol{u}_{\mathrm{m2}} \\ \Delta\boldsymbol{u}_{\mathrm{m3}} \\ \Delta\boldsymbol{u}_{\mathrm{m4}} \\ \Delta\boldsymbol{u}_{\mathrm{g}} \end{array}\right] \tag{22}$$

where the state matrix is denoted as $\boldsymbol{A}$, and its order is 72×72. On the base of the small-signal model, the influences of slope coefficient, PI control parameter, smoothing reactor parameter, and bridge arm inductance on the system stability are analyzed using Lyapunov stability theory and the root locus method.

III. STABILITY ANALYSIS

The Zhangbei Project in Fig. 4 is used to analyze the influences of various parameters, in which the DC voltage sloop control is adopted at the Fengning station and the Beijing station, and the constant active power control is adopted at other two stations. Table 1 shows the main parameters of each converter station. Table 2 shows the main parameters of DC transmission lines.

A. INFLUENCE ANALYSIS OF CONTROL PARAMETERS IN DC VOLTAGE SLOPE CONTROLLER

Taking Fengning station as an example, the influences of the DC voltage slope coefficient and the outer loop PI control parameters on system stability are analyzed.

$$\Delta\boldsymbol{I}_{\mathrm{L}} = \left[\begin{array}{cccc}\Delta I_{12} & \Delta I_{24} & \Delta I_{13} & \Delta I_{34}\end{array}\right]^{\mathrm{T}};$$

$$\Delta\boldsymbol{y}_{\mathrm{g}} = \Delta\boldsymbol{U}_{\mathrm{dc}} = \left[\begin{array}{cccc}\Delta U_{\mathrm{dc1}} & \Delta U_{\mathrm{dc2}} & \Delta U_{\mathrm{dc3}} & \Delta U_{\mathrm{dc4}}\end{array}\right]^{\mathrm{T}};$$

$$\Delta\boldsymbol{u}_{\mathrm{g}} = \left[\begin{array}{cccc}\Delta I_{\mathrm{dc1}} & \Delta I_{\mathrm{dc2}} & \Delta I_{\mathrm{dc3}} & \Delta I_{\mathrm{dc4}}\end{array}\right]^{\mathrm{T}};$$

$$\boldsymbol{A}_{\mathrm{g}} = \left[\begin{array}{cc}\boldsymbol{F}_1 & \boldsymbol{F}_2 \\ \boldsymbol{F}_3 & 0_{4\times4}\end{array}\right]; \boldsymbol{B}_{\mathrm{g}} = \left[\begin{array}{c}0_{4\times4} \\ \boldsymbol{F}_4\end{array}\right]; \boldsymbol{C}_{\mathrm{g}} = \left[\begin{array}{cc}0_{4\times4} & I_{4\times4}\end{array}\right]; \boldsymbol{D}_{\mathrm{g}} = [0]_{4\times4};$$

$$\boldsymbol{F}_1 = \left[\begin{array}{cccc} \dfrac{-R_{12}}{2L_{\mathrm{s12}}+L_{12}} & 0 & 0 & 0 \\ 0 & \dfrac{-R_{13}}{2L_{\mathrm{s13}}+L_{13}} & 0 & 0 \\ 0 & 0 & \dfrac{-R_{24}}{2L_{\mathrm{s24}}+L_{24}} & 0 \\ 0 & 0 & 0 & \dfrac{-R_{34}}{2L_{\mathrm{s34}}+L_{34}} \end{array}\right];$$

$$\boldsymbol{F}_2 = \left[\begin{array}{cccc} \dfrac{1}{2L_{\mathrm{s12}}+L_{12}} & \dfrac{-1}{2L_{\mathrm{s12}}+L_{12}} & 0 & 0 \\ \dfrac{1}{2L_{\mathrm{s13}}+L_{13}} & 0 & \dfrac{-1}{2L_{\mathrm{s13}}+L_{13}} & 0 \\ 0 & \dfrac{1}{2L_{\mathrm{s24}}+L_{24}} & 0 & \dfrac{-1}{2L_{\mathrm{s24}}+L_{24}} \\ 0 & 0 & \dfrac{1}{2L_{\mathrm{s34}}+L_{34}} & \dfrac{-1}{2L_{\mathrm{s34}}+L_{34}} \end{array}\right];$$

$$\boldsymbol{F}_3 = \left[\begin{array}{cccc} \dfrac{-1}{C_{12}+C_{13}} & \dfrac{-1}{C_{12}+C_{13}} & 0 & 0 \\ \dfrac{1}{C_{12}+C_{24}} & 0 & \dfrac{-1}{C_{12}+C_{24}} & 0 \\ 0 & \dfrac{1}{C_{13}+C_{34}} & \dfrac{-1}{C_{13}+C_{34}} & 0 \\ 0 & \dfrac{1}{C_{24}+C_{34}} & 0 & \dfrac{1}{C_{24}+C_{34}} \end{array}\right];$$

$$\boldsymbol{F}_4 = \left[\begin{array}{cccc} \dfrac{1}{C_{12}+C_{13}} & 0 & 0 & 0 \\ 0 & \dfrac{1}{C_{12}+C_{24}} & 0 & 0 \\ 0 & 0 & \dfrac{1}{C_{13}+C_{34}} & 0 \\ 0 & 0 & 0 & \dfrac{1}{C_{24}+C_{34}} \end{array}\right].$$

TABLE 1. Main parameters of converter stations.

Parameter	Kangbao	Fengning	Beijing	Zhangbei
AC voltage/kV	500	500	220	220
DC voltage/kV	±500	±500	±500	±500
Capacity/MW	1700	1700	3400	3400
Sub-module number/N	200	200	200	200

TABLE 2. Main parameters of DC transmission lines.

Line	Kangbao-Zhangbei	Kangbao-Fengning	Zhangbei-Beijing	Fengning-Beijing
Distance/km	50	200	208	180
Resistance /Ω	0.48	2.02	2.01	1.84
Inductance/H	0.04	0.175	0.174	0.16
Capacitance/μF	0.34	1.41	1.41	1.28

1) THE DC VOLTAGE SLOPE COEFFICIENT

Improper values of slope coefficients will directly affect the voltage compensated values required by each converter stations to meet the system stability, resulting in the system instability. Suppose that the slope coefficient k in Fig. 2 increases from 0.1 to 1 at step 0.01, and other control parameters remain unchanged. Fig. 5 shows the root locus of dominant poles when the slope k changes.

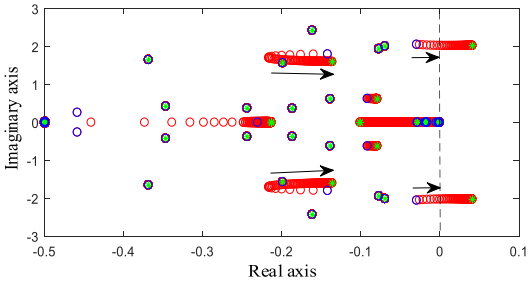

FIGURE 5. Root locus of dominant poles when the slope k changes.

In Fig. 5, as the slope coefficient k increases, the root locus of dominant poles moves from the left-half to the right-half on the complex plane. When $k = 0.25$, the root locus crosses the imaginary axis, and the system loses stability. Therefore, the value of the slope parameter k must be less than 0.25 if the system keeps stable in this example.

2) THE OUTER LOOP PI CONTROL PARAMETERS

In Fig. 2, suppose that the outer loop proportional gain k_{pp} increases from 10 to 20 at step 0.1, the integral gain k_{ip} increases from 0.1 to 10 at step 0.1, respectively. Other parameters remain unchanged. Fig. 6 shows the root locus diagrams of their dominant poles when they change separately.

As seen in Fig. 6, when the outer loop proportional gain k_{pp} increases, its root locus of dominant poles moves from the left-half to the right-half on the complex plane. When $k_{pp} = 17.8$, the root locus crosses the imaginary axis, the system loses stability. Hence, the value of the proportional gain k_{pp} must be less than 17.8 for the system stability in this example. But the integral gain k_{ip} increases, its root locus of dominant poles always remain on the left-half plane, and move away from the imaginary axis, enhancing the system stability.

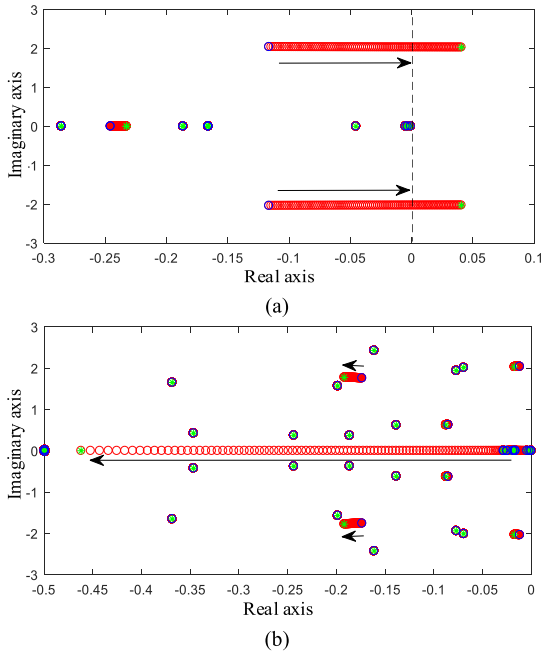

FIGURE 6. Root locus of PI control parameters at Fengning station. (a) Proportional gain k_{pp} and (b) integral gain k_{ip}.

B. INFLUENCE ANALYSIS OF CIRCULATION SUPPRESSOR CONTROL PARAMETERS

Take Kangbao Station as an example to analyze the influence of control parameters in the circulating current suppressor on the stability of the system. In Fig. 3, suppose that the proportional gain k_{p2} increases from 10 to 15 at step 0.1, and the integral gain k_{i2} increases from 5 to 10 at step 0.1, respectively. Other parameters remain unchanged. Fig. 7 shows the root locus of the modes related to the double frequency circulating current when they change separately.

In Fig. 7(a), as the proportional gain k_{p2} increases, its root locus of the modes related to the double frequency circulating current moves on the left-half plane and is gradually away from the imaginary axis. This shows that the corresponding modes of the double frequency circulating current enhance the system stability and weaken the suppression effect on the circulating current.

In Fig. 7(b), as the integral gain k_{i2} increases, its root locus of the modes related to the double frequency circulating current still moves on the left-half plane and gradually approaches the imaginary axis. The results show that the corresponding modes of the double frequency circulating current only weaken the system stability and enhance the suppression effect on the circulating current.

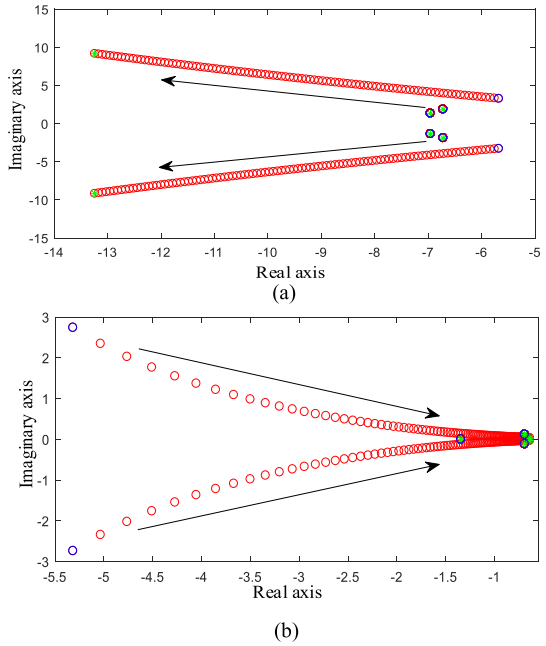

FIGURE 7. Root locus of the double-frequency circulating current at Kangbao station. (a) Proportional gain k_{p2} and (b) integral gain k_{i2}.

C. INFLUENCE ANALYSIS OF SMOOTHING REACTOR PARAMETER

The selection of the smoothing reactor parameter should not only take into account the effect of the DC current harmonic suppression, but also ensure the system stability. Suppose that smoothing reactor parameters L_s in Fig. 4 gradually increases from 0.1H to 0.7H at step 0.01H. Fig. 8 shows the root locus diagram of dominant poles when L_s changes.

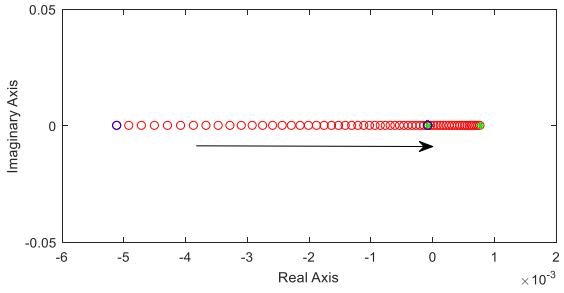

FIGURE 8. Root locus of dominant pole when L_s changes.

As seen in Fig. 8, the root locus of dominant pole moves from the left-half to the right-half on the complex plane. When $L_s = 0.48$H, the root locus crosses the imaginary axis, and the system loses the stability. Thus, the value of the smoothing reactor L_s must be less than 0.48H if the system keeps stable in this example.

D. INFLUENCE ANALYSIS OF MMC BRIDGE ARM INDUCTANCE

The upper and lower bridge arm reactors of MMC are used to suppress the interphase circulation caused by the bridge arms' voltage imbalance, and inappropriate parameters will also affect the stability of the system. Taking the Kangbao station as an example, the influence of MMC bridge arm inductance on the system stability is analyzed. Set that the inductance L_{arm} of the three-phase bridge arms in Fig. 1 increases from 0.05H to 0.5H at 0.01H step. Fig.9 shows the root locus of dominant pole when L_{arm} changes.

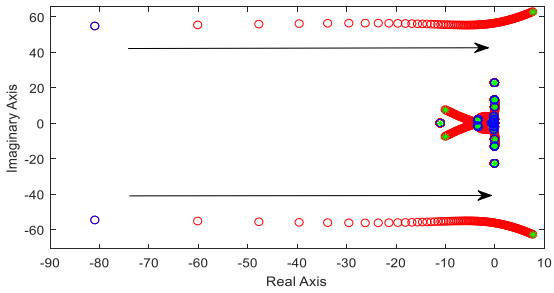

FIGURE 9. Root locus of dominant poles when L_{arm} changes.

In Fig.9, as the inductance L_{arm} increases, the root locus of dominant poles also moves from the left-half to the right-half on the complex plane. When the inductance L_{arm} is more than 0.39H, the system loses stability. Hence, the selection of the MMC bridge arm inductance L_{arm} must be less than 0.39H for the system stability in this example.

IV. SIMULATION

To testify the correctness of the presented small-signal model and the conclusions about the impact of various parameters on the system stability, the simulation of the Zhangbei project in China is established via PSCAD/EMTDC platform. The simulation time is 5s. Under the initial conditions, the Kangbao station sends 1500MW, the Zhangbei station sends 3000MW, the Fengning station receives 1500MW and the Beijing station receives 3000MW.

A. SIMULATION OF SLOPE COEFFICIENT IN DC VOLTAGE SLOPE CONTROLLER

Unreasonable selection of the slope coefficient k will affect the stability of the system. In *A* of Section III, the conclusion of the stability analysis is given, that is, the slope parameter k must be less than 0.25 if the system keeps stable. Taking Fengning station as an example, the slope coefficient k is set as 0.1 and 0.3, respectively. When the power of Fengning station drops from 1500MW to 1200MW in 3s, the power waveforms with different k values at Fengning station are shown in Fig. 10.

As seen in Fig. 10(a), the active power waveform at Fengning station can quickly track a given value 1200WM after 3s, the overshoot of waveform is very small and the transient time is very short, when the slope coefficient k is set as 0.1. In this case, the system still remains stable. In Fig. 10(b), the overshoot of waveform reaches 200MW, the active power receiving has deviated from the given value 1200MW and always oscillates after 3s, when the slope coefficient k is set as

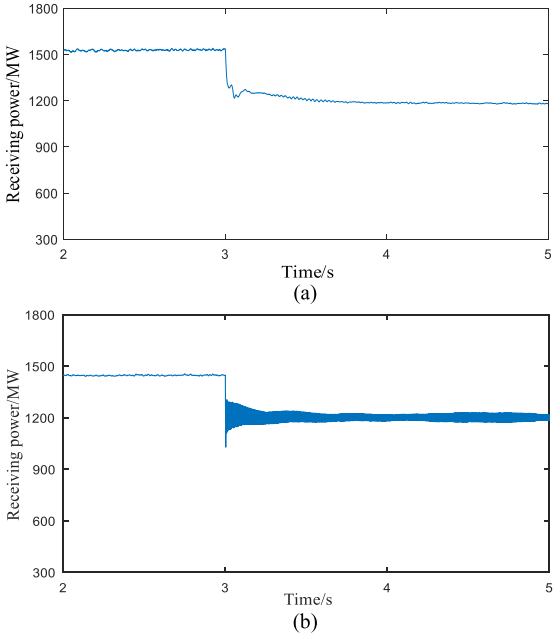

FIGURE 10. Waveform comparisons at Fengning station with different slope coefficients (a) Slope coefficient k=0.1 and (b) slope coefficient k=0.3.

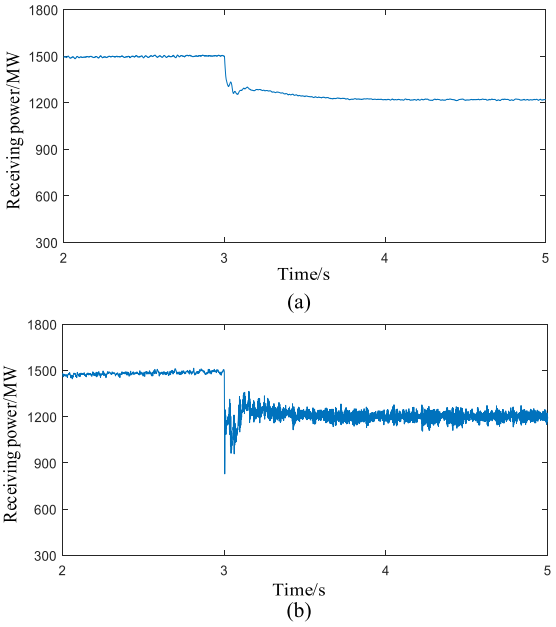

FIGURE 11. Waveform comparisons at Fengning station with different outer loop proportional gains. (a) Proportional gain k_{pp} = 10 and (b) proportional gain k_{pp} = 18.

0.3. In this case, the system is unstable so that it cannot reach a new stable state. This simulation proves that the conclusion about the slope coefficient k in *A* of Section III is correct.

B. SIMULATION OF OUTER LOOP PROPORTIONAL GAIN IN DC VOLTAGE SLOPE CONTROLLER

Improper selection of the outer loop proportional gain in the DC voltage slope controller will also affect the stability of the system. In *A* of Section III, the conclusion of the stability analysis is given, that is, the value of the proportional gain k_{pp} must be less than 17.8 if the system keeps stable. Taking Fengning station as an example, the proportional gain k_{pp} in the DC voltage slope controller is set as 10 and 18, respectively. When the receiving power at Fengning station drops from 1500MW to 1200MW in 3s, the active power waveforms with different k_{pp} value at Fengning station are shown in Fig.11.

As seen in Fig. 11(a), the power waveform can quickly track a given value 1200MW after 3s, the overshoot of waveform is very small and the transient time is very short, when the proportional gain k_{pp} is set as 10. In this case, the system still keeps stable. In Fig.11(b), the overshoot of waveform is more than 300MW, and the waveform oscillates seriously after 3s, when the proportional gain k_{pp} is set as 18. In this case, the system losses its stability. This simulation proves that the conclusion about the outer loop proportional gain k_{pp} of the DC voltage slope controller in *A* of Section III is correct.

C. SIMULATION OF PI CONTROL PARAMETERS IN CIRCULATION CURRENT SUPPRESSOR

In order to prove that control parameters in the circulating current suppressor have the effect of restraining the circulating current and have litter effect on the system stability, take Kangbao station as the tested object. The circulating current suppressor doesn't run at the initial time. When the system runs to 2s, put the circulating current suppressor into operation. When the system runs to 3s, change control parameters of the suppressor. The circulating current waveforms in the three cases are compared.

1) SIMULATION OF PROPORTIONAL GAIN IN THE CIRCULATION CURRENT SUPPRESSOR

Suppose that the initial value of the proportional gain k_{p2} is set to 10. When the system runs to 3s, the proportional gain k_{p2} is set as 30, and other parameters remain unchanged. Fig.12 shows the double frequency circulating current waveform in the three cases at the Kangbao station.

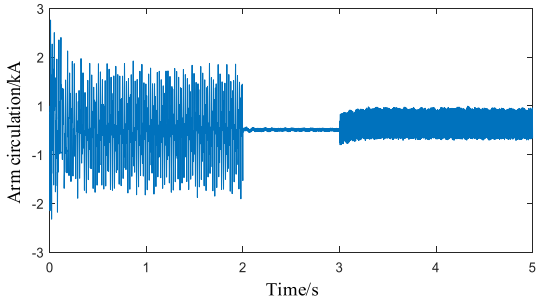

FIGURE 12. Waveform of circulating current with no suppressor and different proportional gain k_{p2}.

In Fig.12, the circulating current is changed between [−1.5, 1.5] kA before 2s, and its amplitude is relatively large. The circulating current suppressor runs after 2s, the

circulating current decreases, and this shows that the circulating current suppressor can effectively suppress the circulating current. Moreover, when the proportional gain k_{p2} is increased from 10 to 30 at 3s, the circulating current is changed from zero to [−0.5, 0.5] kA, and the circulating current suppression effect is weakened.

2) SIMULATION OF INTEGRAL GAIN IN THE CIRCULATION CURRENT SUPPRESSOR

When the system runs to 2s, the circulating current suppressor puts into operation, and the initial value of its integral gain k_{i2} is set as 5. When the system runs to 3s, the integral gain k_{i2} is increased to 10, and other parameters remain unchanged. Fig.13 shows the double frequency circulating current waveform in the three cases at the Kangbao station.

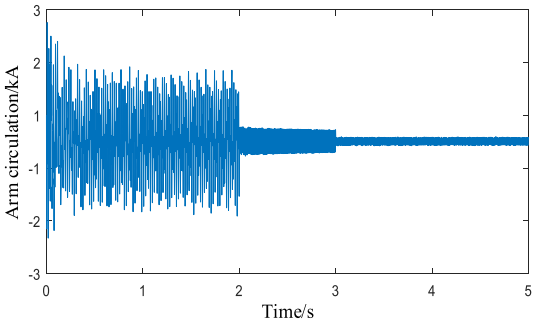

FIGURE 13. Waveform of circulating current with no suppressor and different integral gain k_{i2}.

In Fig.13, the circulating current suppressor runs after 2s, the circulating current decreases, and this shows that the circulating current suppressor can effectively suppress the circulating current. Moreover, when the proportional gain k_{i2} is increased from 5 to 10 at 3s, the circulating current is changed from [−0.6, 0.6] to [−0.1, 0.1] kA, and the circulating current suppression effect is enhanced.

The above verifies the correctness of the conclusions about control parameters of the circulating current suppressor in *B* of Sections III.

D. SIMULATION OF SMOOTHING REACTOR PARAMETERS

Unreasonable selection of smoothing reactor parameter L_s will affect the stability of the system. In *C* of Section III, the conclusion of the stability analysis is given, that is, the parameter L_s must be less than 0.48H if the system remains stable. Suppose that the smoothing reactor parameters L_s are set as 0.2H and 0.5H, respectively. When the system runs to 3s, the received power at Beijing station step from 3000WM to 3300MW. The received power waveforms at Beijing station under different smoothing reactors are shown in Fig. 14.

As shown in Fig. 14(a), the received power at Beijing station can accurately track a given value after 3s and the system still remains stable, when the smoothing reactor parameters L_s are 0.2H. In Fig. 14(b), when the parameters L_s are 0.5H,

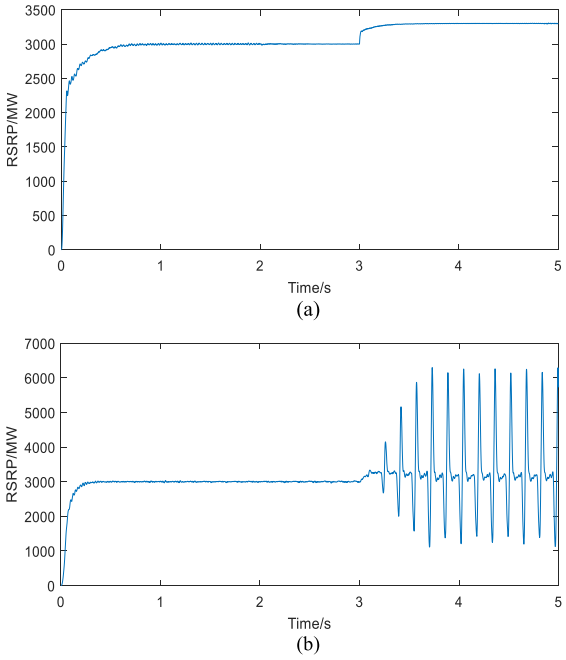

FIGURE 14. Waveforms of received power at Beijing station with different smoothing reactor L_s. (a) Smoothing reactor L_s is 0.2H and (b) smoothing reactor L_s is 0.5H.

the received power fluctuates greatly after 3s, resulting in the system instability. The simulation verifies the correctness of the conclusion about smoothing reactor parameters in *C* of Section III.

V. CONCLUSION

By studying the interaction mechanism between converter stations using the DC voltage slope control and DC girds with smoothing reactors, this paper develops a comprehensive small-signal stability model of the MMC-based DC grid, which also includes the internal dynamic behaviors of MMCs and the circulating current suppressor. The proposed method provides some theoretical guidance for the system design and the parameter selection in DC grid applications as follows.

1) The slope coefficient has a great influence on the system stability and power balance. When the slope coefficient exceeds a certain threshold, the active power fluctuations at the converter station increase significantly, resulting in the system instability.
2) The outer loop proportional gain of the DC voltage slope controller has a certain influence on the system stability. If the proportional gain exceeds a threshold value, the system will be unstable.
3) The values of the smoothing reactor and MMC bridge arm reactor will also affect the system stability. The system will lose stable when these two parameters exceed their respective thresholds.
4) The PI control parameters of the circulating current suppressor doesn't only affect the system stability, but also have an impact on the suppression effect of the double frequency circulating current.

$$
\boldsymbol{A_s} = \begin{bmatrix}
0 & 0 & 0 & 0 & 0 & \frac{1}{6C} & \frac{U_{c1d0}}{4CU_{dc0}} & \frac{U_{c1q0}}{4CU_{dc0}} & \frac{U_{cird0}}{2CU_{dc0}} & \frac{U_{cirq0}}{2CU_{dc0}} \\
0 & 0 & -\omega_0 & 0 & 0 & \frac{-U_{c1d0}}{3CU_{dc0}} & \frac{-U_{dc0}-U_{cird0}}{4CU_{dc0}} & \frac{-U_{cirq0}}{4CU_{dc0}} & \frac{-U_{c1d0}}{2CU_{dc0}} & \frac{-U_{c1q0}}{2CU_{dc0}} \\
0 & \omega & 0 & 0 & 0 & \frac{-U_{c1q0}}{3CU_{dc0}} & \frac{-U_{cirq0}}{4CU_{dc0}} & \frac{-U_{dc0}+U_{cird0}}{4CU_{dc0}} & \frac{U_{c1q0}}{2CU_{dc0}} & \frac{-U_{c1d0}}{2CU_{dc0}} \\
0 & 0 & 0 & 0 & -2\omega_0 & \frac{U_{cird0}}{3CU_{dc0}} & \frac{U_{c1d0}}{4CU_{dc0}} & \frac{-U_{c1q0}}{4CU_{dc0}} & \frac{1}{2C} & 0 \\
0 & 0 & 0 & 2\omega_0 & 0 & \frac{U_{cirq0}}{3CU_{dc0}} & \frac{U_{c1q0}}{4CU_{dc0}} & \frac{U_{c1d0}}{4CU_{dc0}} & 0 & \frac{1}{2C} \\
\frac{-3N}{2L_{arm}} & \frac{3NU_{c1d0}}{2L_{arm}U_{dc0}} & \frac{3NU_{c1q0}}{2L_{arm}U_{dc0}} & \frac{-3NU_{cird0}}{2L_{arm}U_{dc0}} & \frac{-3NU_{cirq0}}{2L_{arm}U_{dc0}} & \frac{-R_{arm}}{L_{arm}} & 0 & 0 & 0 & 0 \\
\frac{-2NU_{c1d}}{2L_{eq}U_{dc}} & \frac{NU_{cird}+NU_{dc}}{2L_{eq}U_{dc}} & \frac{NU_{cirq0}}{2L_{eq}U_{dc0}} & \frac{-NU_{c1d0}}{2L_{eq}U_{dc0}} & \frac{-NU_{c1q0}}{2L_{eq}U_{dc0}} & 0 & \frac{-R_{eq}}{L_{eq}} & -\omega_0 & 0 & 0 \\
\frac{-2NU_{c1q0}}{2L_{eq}U_{dc0}} & \frac{NU_{cirq0}}{2L_{eq}U_{dc0}} & \frac{NU_{dc0}-NU_{cird0}}{2L_{eq}U_{dc0}} & \frac{NU_{c1q0}}{2L_{eq}U_{dc0}} & \frac{-NU_{c1d0}}{2L_{eq}U_{dc0}} & 0 & \omega_0 & \frac{-R_{eq}}{L_{eq}} & 0 & 0 \\
\frac{-NU_{cird0}}{L_{arm}U_{dc0}} & \frac{NU_{c1d0}}{2L_{arm}U_{dc0}} & \frac{-NU_{c1q0}}{2L_{arm}U_{dc0}} & \frac{-N}{2L_{arm}} & 0 & 0 & 0 & 0 & \frac{-R_{arm}}{L_{arm}} & -2\omega_0 \\
\frac{-NU_{cirq0}}{L_{arm}U_{dc0}} & \frac{NU_{c1q0}}{2L_{arm}U_{dc0}} & \frac{NU_{c1d0}}{2L_{arm}U_{dc0}} & 0 & \frac{-N}{2L_{arm}} & 0 & 0 & 0 & 2\omega_0 & \frac{-R_{arm}}{L_{arm}}
\end{bmatrix} \tag{A1}
$$

$$
\boldsymbol{B_s} = \begin{bmatrix}
0 & 0 & 0 & 0 & \frac{I_{sd0}}{4CU_{dc0}} & \frac{I_{sq0}}{4CU_{dc0}} & \frac{I_{cird0}}{2CU_{dc0}} & \frac{I_{cirq0}}{2CU_{dc0}} \\
0 & 0 & 0 & -U_{c\_1q0} & \frac{-2I_{dc0}-3I_{cird0}}{6CU_{dc0}} & \frac{-I_{cirq0}}{2CU_{dc0}} & \frac{-I_{sd0}}{4CU_{dc0}} & \frac{-I_{sq0}}{4CU_{dc0}} \\
0 & 0 & 0 & U_{c\_1d0} & \frac{-I_{cirq0}}{2CU_{dc0}} & \frac{3I_{cird0}-2I_{dc0}}{6CU_{dc0}} & \frac{I_{sq0}}{4CU_{dc0}} & \frac{-I_{sd0}}{4CU_{dc0}} \\
0 & 0 & 0 & -2U_{c\_2q0} & \frac{I_{sd0}}{4CU_{dc0}} & \frac{-I_{sq0}}{4CU_{dc0}} & \frac{I_{dc0}}{3CU_{dc0}} & 0 \\
0 & 0 & 0 & 2U_{c\_2d0} & \frac{I_{sq0}}{4CU_{dc0}} & \frac{I_{sd0}}{4CU_{dc0}} & 0 & \frac{I_{dc0}}{3CU_{dc0}} \\
0 & 0 & \frac{3}{2L_{arm}} & 0 & \frac{3NU_{c\_1d0}}{2L_{arm}U_{dc0}} & \frac{3NU_{c\_1q0}}{2L_{arm}U_{dc0}} & \frac{-3NU_{c\_2d0}}{2L_{arm}U_{dc0}} & \frac{-3NU_{c\_2q0}}{2L_{arm}U_{dc0}} \\
\frac{1}{L_{eq}} & 0 & 0 & -I_{sq0} & \frac{-2NU_{c\_dc}-NU_{c\_2d}}{2L_{eq}U_{dc}} & \frac{-NU_{c\_2q}}{2L_{eq}U_{dc}} & \frac{NU_{c\_1d0}}{2L_{eq}U_{dc0}} & \frac{NU_{c\_1q0}}{2L_{eq}U_{dc0}} \\
0 & \frac{1}{L_{eq}} & 0 & I_{sd0} & \frac{-NU_{c\_2q0}}{2L_{eq}U_{dc0}} & \frac{-2NU_{c\_dc0}+NU_{c\_2d0}}{2L_{eq}U_{dc0}} & \frac{-NU_{c\_1q0}}{2L_{eq}U_{dc0}} & \frac{NU_{c\_1d0}}{2L_{eq}U_{dc0}} \\
0 & 0 & 0 & -2I_{cirq0} & \frac{NU_{c\_1d0}}{2L_{arm}U_{dc0}} & \frac{-NU_{c\_1q0}}{2L_{arm}U_{dc0}} & \frac{-NU_{c\_dc0}}{L_{arm}U_{dc0}} & 0 \\
0 & 0 & 0 & 2I_{cird0} & \frac{NU_{c\_1q0}}{2L_{arm}U_{dc0}} & \frac{NU_{c\_1d0}}{2L_{arm}U_{dc0}} & 0 & \frac{-NU_{c\_dc0}}{L_{arm}U_{dc0}}
\end{bmatrix} \tag{A2}
$$

In this paper, the balanced condition is only considered. In fact, the unbalance condition is a more practical event. In the case of unbalance condition, the AC current on the MMC valve side will has a negative-sequence component of fundamental frequency, and the bridge arm currents of the MMC converter will appear the zero-sequence double-frequency circulating currents [27]. The stability analysis of MMC-based DC grids under unbalanced AC system is the future work.

APPENDIX

The coefficient matrices $\boldsymbol{A_s}$ and $\boldsymbol{B_s}$, as shown at the top of the page, of Eq. (11) are shown as follows, respectively.

REFERENCES

[1] A. Jain, O. Saborío-Romano, J. N. Sakamuri, and N. A. Cutululis, "Black-start from HVDC-connected offshore wind: Hard versus soft energization," *IET Renew. Power Gener.*, vol. 15, no. 1, pp. 127–138, Jan. 2021.

[2] D. Shu, V. Dinavahi, X. Xie, and Q. Jiang, "Shifted frequency modeling of hybrid modular multilevel converters for simulation of MTDC grid," *IEEE Trans. Power Del.*, vol. 33, no. 3, pp. 1288–1298, Jun. 2018.

[3] D. Karwatzki and A. Mertens, "Generalized control approach for a class of modular multilevel converter topologies," *IEEE Trans. Power Electron.*, vol. 33, no. 4, pp. 2888–2900, Apr. 2018.

[4] N. Lin and V. Dinavahi, "Variable time-stepping modular multilevel converter model for fast and parallel transient simulation of multiterminal DC grid," *IEEE Trans. Ind. Electron.*, vol. 66, no. 9, pp. 6661–6670, Sep. 2019.

[5] A. Elserougi, I. Abdelsalam, A. Massoud, and S. Ahmed, "A modular multilevel DC–DC converter with self-energy equalization for DC grids," *IET Renew. Power Gener.*, vol. 15, no. 8, pp. 1736–1747, Jun. 2021.

[6] J. Xu, Y. Lu, C. Zhao, and J. Liang, "A model-based DC fault location scheme for multi-terminal MMC-HVDC systems using a simplified transmission line representation," *IEEE Trans. Power Del.*, vol. 35, no. 1, pp. 386–395, Feb. 2020.
[7] H. Pang and X. Wei, "Research on key technology and equipment for Zhangbei 500 kV DC grid," in *Proc. Int. Power Electron. Conf.*, Niigata, Japan, May 2018, pp. 2343–2351.
[8] G. Qiang, Y. Xi, and L. Ye, "Circulating current suppressing and AC faults ride-through capability analysis of Zhoushan MMC-MTDC system," in *Proc. 2nd IEEE Conf. Energy Internet Energy Syst. Integr.*, Beijing, China, Oct. 2018, pp. 1–6.
[9] S. P. Teeuwsen, "Modeling the trans bay cable project as voltage-sourced converter with modular multilevel converter design," in *Proc. IEEE Power Energy Soc. Gen. Meeting*, Detroit, MI, USA, Jul. 2011, pp. 1–8.
[10] D. C. Ludois and G. Venkataramanan, "Simplified terminal behavioral model for a modular multilevel converter," *IEEE Trans. Power Electron.*, vol. 29, no. 4, pp. 1622–1631, Apr. 2014.
[11] J. Sun and H. Liu, "Sequence impedance modeling of modular multilevel converters," *IEEE J. Emerg. Sel. Topics Power Electron.*, vol. 5, no. 4, pp. 1427–1442, Dec. 2017.
[12] A. Jamshidifar and D. Jovcic, "Small-signal dynamic DQ model of modular multilevel converter for system studies," *IEEE Trans. Power Del.*, vol. 31, no. 1, pp. 191–199, Feb. 2016.
[13] G. Bergna, J. Suul, and S. D'Arco, "Small-signal state-space modeling of modular multilevel converters for system stability analysis," in *Proc. IEEE Energy Convers. Congr. Expo.*, Montreal, QC, Canada, Oct. 2015, pp. 5822–5829.
[14] J. Hu, J. Zhu, and M. Wan, "Modeling and analysis of modular multilevel converter in DC voltage control timescale," *IEEE Trans. Ind. Electron.*, vol. 66, no. 8, pp. 6449–6459, Aug. 2019.
[15] J. Freytes, G. Bergna, J. Suul, S. D'Arco, F. Gruson, F. Colas, H. Saad, and X. Guillaud, "Improving small-signal stability of an MMC with CCSC by control of the internally stored energy," *IEEE Trans. Power Del.*, vol. 33, no. 1, pp. 429–439, Feb. 2018.
[16] J. Lyu, X. Zhang, X. Cai, and M. Molinas, "Harmonic state-space based small-signal impedance modeling of a modular multilevel converter with consideration of internal harmonic dynamics," *IEEE Trans. Power Electron.*, vol. 34, no. 3, pp. 2134–2148, Mar. 2019.
[17] Q. Hao, Z. Li, F. Gao, and J. Zhang, "Reduced-order small-signal models of modular multilevel converter and MMC-based HVDC grid," *IEEE Trans. Ind. Electron.*, vol. 66, no. 3, pp. 2257–2268, Mar. 2019.
[18] Y. Li, G. Tang, J. Ge, Z. He, H. Pang, J. Yang, and Y. Wu, "Modeling and damping control of modular multilevel converter based DC grid," *IEEE Trans. Power Syst.*, vol. 33, no. 1, pp. 723–735, Jun. 2018.
[19] Z. Li, Z. Wang, Y. Wang, T. Yin, N. Mei, B. Yue, and W. Lei, "Accurate impedance modeling and control strategy for improving the stability of DC system in multiterminal MMC-based DC grid," *IEEE Trans. Power Electron.*, vol. 35, no. 10, pp. 10026–10049, Oct. 2020.
[20] G.-S. Lee, D.-H. Kwon, and S.-I. Moon, "DC current and voltage droop control method of hybrid HVDC systems for an offshore wind farm connection to enhance AC voltage stability," *IEEE Trans. Energy Convers.*, vol. 36, no. 1, pp. 468–479, Mar. 2021.
[21] S. Li, W. Chen, X. Yin, D. Chen, and Y. Teng, "A novel integrated protection for VSC-HVDC transmission line based on current limiting reactor power," *IEEE Trans. Power Del.*, vol. 35, no. 1, pp. 226–233, Feb. 2020.
[22] B. Li, J. He, Y. Li, and R. Li, "A novel solid-state circuit breaker with self-adapt fault current limiting capability for LVDC distribution network," *IEEE Trans. Power Electron.*, vol. 34, no. 4, pp. 3516–3529, Apr. 2019.
[23] M. Song, T. Ma, C. Sheng, S. Dai, L. Zhong, X. Duan, and L. Li, "The parameter design and system simulation of 160-kV/1-kA resistive-type superconducting DC fault current limiter," *IEEE Trans. Appl. Supercond.*, vol. 29, no. 5, Aug. 2019, Art. no. 5603706.
[24] P. Wang, Y. Zhao, F. Lv, K. Li, and Y. Ding, "Distribution of electric field and structure optimisation on the surface of a ± 1100 kV smoothing reactor," *IET Sci., Meas. Technol.*, vol. 13, no. 3, pp. 441–446, May 2019.
[25] D. J. Melvold and W. F. Long, "Back-to-back HVDC system performance with different smoothing reactors," *IEEE Trans. Power Del.*, vol. 4, no. 1, pp. 208–215, Jan. 1989.
[26] J. Bin-Kai and W. Zhi-Xin, "Study on an improved DC voltage slope control strategy for VSC-MTDC," in *Proc. IEEE 7th Int. Conf. Power Energy Syst. (ICPES)*, Toronto, ON, Canada, Nov. 2017, pp. 57–61.
[27] Q. Hao, Z. Li, C. Yue, F. Gao, and S. Wang, "Small-signal model and dynamics of MMC-HVDC grid under unbalanced grid conditions," *IEEE Trans. Power Del.*, vol. 36, no. 5, pp. 3172–3184, Oct. 2021.

HUI LI was born in Hubei, China, in 1976. She received the B.E. and Ph.D. degrees from China Agricultural University, Beijing, China, in 2000 and 2005, respectively.

She is currently a Professor with the School of Automation, Beijing Information Science & Technology University. Her research interests include modeling and control of flexible HVDC transmission systems, and renewable power generation technology.

XINQIAO FAN was born in Hebei, China, in 1982. He received the Ph.D. degree from North China Electric Power University, China, in 2012.

From 2012 to 2015, he was an Engineer with the State Grid Electric Power Research Institute, China. He is currently an Assistant Professor with the School of Automation, Beijing Information Science & Technology University. His research interests include traveling-wave-based fault location of transmission lines and power systems stability analysis.

SIJIA LIU was born in Xi'an, China, in 1986. He received the B.E. degree from Tsinghua University, in 2008, and the Ph.D. degree from Beijing Jiaotong University, in 2017.

He worked as an Engineer at the Beijing Construction Engineering Group (BCEG), from 2009 to 2011. He is currently an Assistant Professor with the School of Automation, Beijing Information Science & Technology University. His research interests include linear induction motor and nonlinear systems control.